Applied Catalysis B: Environmental 307 (2022) 121141

Contents lists available at ScienceDirect

Applied Catalysis B: Environmental

journal homepage: www.elsevier.com/locate/apcatb

Tailoring the oxidation state of metallic TiO through Ti^{3+}/Ti^{2+} regulation for photocatalytic conversion of CO_2 to C_2H_6

Baoxin Ni [a], Hua Jiang [a], WenYao Guo [a], Qunjie Xu [a,b], Yulin Min [a,b,*]

[a] Shanghai Key Laboratory of Materials Protection and Advanced Materials Electric Power, Shanghai Engineering Research Center of Energy-Saving in Heat Exchange Systems, Shanghai University of Electric Power, Shanghai 200090, PR China

[b] Shanghai Institute of Pollution Control and Ecological Security, Shanghai 200092, PR China

ARTICLE INFO

Keywords:
Oxidation state
TiO
Metallic photocatalyst
Co-doping
Photocatalytic CO_2 conversion
C_2H_6

ABSTRACT

The regulation and stabilization of the oxidation state to promote the conversion of CO_2 to C_2 fuel still faces many challenges. Based on the principle of charge balance, we creatively propose a co-doping strategy to adjust the surface oxidation state distribution of metallic catalysts. A TiO-based photocatalyst co-doped with Zn and N was synthesized by ammonia assisted one-step calcination method, named ZN-TC. XPS characterization shows that Zn and N adjust the valence states of adjacent Ti elements respectively, so that the surface of TiO maintains a relatively stable Ti^{3+}/Ti^{2+} ratio. Under visible light irradiation, the material can catalyze CO_2 into CO (324.11 $\mu mol \cdot g^{-1} \cdot h^{-1}$) and C_2H_6 (10.27 $\mu mol \cdot g^{-1} \cdot h^{-1}$) in the liquid phase. The selectivity of C_2H_6 reached 14.45%. When irradiated with near-infrared light, ZN-TC shows 100% CO selectivity because the photon energy is not enough to support the catalytic hydrogenation of CO_2. Theoretical calculations and experiments proved that Zn and N elements mainly act on the B_{-1} band to regulate the Ti valence state. In-situ DRIFTS and in-situ Raman tests confirmed the function of oxidation state adjustment to promote the C-C coupling on the catalyst surface to produce ethoxy groups, which ultimately led to the production of C_2H_6.

1. Introduction

The photocatalytic reduction of carbon dioxide (CO_2RR) provides a sustainable and environmental pathway to produce high-value multi-carbon (C_{2+}) fuels [1]. However, despite the current works possessing highly selective CO_2 reduction, the efficient conversion of CO_2 multi-carbon products and the obscure active site-performance relationship are still the main bottlenecks that limit its development. As the highest oxidation state of carbon, the high dissociation energy of the carbon-oxygen double bond (750 KJ/mol) brings great challenges to CO_2 adsorption, continuous protonation and subsequent C-C coupling [1–3]. Specifically, the reduction of CO_2 is a multi-electron reaction in which different numbers of electrons and protons correspond to different reaction intermediates. Represented by ethane, which has a higher energy density, the conversion of carbon dioxide to ethane is a 14-electron reaction, which theoretically occurs at − 0.51 V (vs NHE) [2]. During the generation of ethane, metal sites are required to provide high-density carriers to promote C-C coupling and stabilize the key intermediate $CH_3CH_2O^*$. However, the appearance of the intermediate CH_3CHO^* will inevitably lead to the production of ethylene, which severely reduces the C_2 selectivity [2]. In addition, Xu et al. [4] recently discovered that the hydrogenation reaction of CO* with adsorbed water is more likely to be the rate-determining step (RDS) compared to the C-C coupling step, and their competition for active sites will lead to a change in the order of reaction. Therefore, exploring the effect of active site properties on hydrogenation and C-C coupling is of great significance for the photoreduction of CO_2 to C_2 fuel.

Recently, it has been proposed that the oxidation state of the active site can affect the activity and selectivity of CO_2RR [5]. The change of oxidation state causes electron redistribution and regulates the splitting of the ligand field and D-orbital, thereby changing the spin state, work function, acidity and energy band structure [5,6]. Research results have shown that the ratio of single active sites has a linear relationship with catalytic activity, such as Ti^{3+} and Cu^{1+} [7,8]. Further studies have found that a single element can increase the yield by adjusting the surface oxidation state to form polarization sites, such as Co^{2+}/Co^{3+}, Ti^{3+}/Ti^{4+}, Bi^{0+}/Bi^{3+} [9–11]. Xu et al. [12] designed a Cu(0)-Cu(I) series catalyst based on poly(ionic liquid) (PIL) to produce C_{2+} products with

* Corresponding author at: Shanghai Key Laboratory of Materials Protection and Advanced Materials Electric Power, Shanghai Engineering Research Center of Energy-Saving in Heat Exchange Systems, Shanghai University of Electric Power, Shanghai 200090, PR China.

E-mail addresses: guowenyao@shiep.edu.cn (W. Guo), ahaqmylin@126.com (Y. Min).

https://doi.org/10.1016/j.apcatb.2022.121141
Received 1 November 2021; Received in revised form 4 January 2022; Accepted 21 January 2022
Available online 25 January 2022
0926-3373/© 2022 Elsevier B.V. All rights reserved.

high reaction rate and high selectivity. Xie et al. [3] further constructed the ternary polarization site of phenakites, and its photocatalytic CO_2 reduction to acetic acid selectivity was as high as 66.9%. Nevertheless, the current research mainly focuses on the exploration of the relationship between activity and oxidation state. In contrast, the relationship between single-element multivalent states and activity has not been systematically explained. For example, titanium has multiple sets of valence states + 2-+ 4. Most of the work focuses on the comparison between the + 3 and the + 4 valence state while few work reports the influence of the + 2 valence state. Besides, the oxidation state faces the problem of transition from active to inactive [13]. or example, Cu_2O undergoes both photoelectron reduction and hole oxidation in the material [1]. The difference in the migration rate of electrons and holes will inevitably cause one of them to accumulate over time, which will eventually lead to an increase in inactive oxidation states and catalyst deactivation. How to effectively suppress this inactivation phenomenon remains to be summarized.

Interestingly, Chen et al. [14] reported the modification of atomically dispersed Ru onto a nickel-vanadium (Ni_3V) layered double hydroxide (LDH) scaffold through strong atomic metal-support interactions. The strong metal-support interaction provided by the nickel-vanadium LDH can stabilize the Ru sites of the reactive atoms, so that the oxidation state fluctuates little on the cathode HER. Inspired by this work, we creatively proposed a co-doping strategy based on the principle of charge balance to regulate the surface oxidation state of metallic titanium monoxide. A titanium monoxide-based photocatalyst co-doped with Zn and N was synthesized by ammonia assisted one-step calcination method, called ZN-TC. The + 2 valence state Zn element and the + 3 valence state N element successfully controlled the valence state distribution of the surrounding local titanium element. Due to the charge difference between the dopant and the lattice oxygen or titanium, the Zn and N co-doping strategy can compensate for the unbalanced charge, thereby reducing the carrier recombination center and forming a new in-band absorption edge. The metal-like properties of titanium monoxide provide high-density carriers, and the particle size of 20 nm also ensures the exposure of more coordinated unsaturated active sites. Therefore, the catalyst can maintain a stable Ti^{3+}/Ti^{2+} ratio and catalyze the conversion of CO_2 to ethane (C_2H_6) with a selectivity of 14.45%.

2. Experimental section

2.1. Materials

Polyacrylonitrile (PAN, MW = 10 W) was provide by Aladdin Regent, Shanghai. N, N-Dimethylformamide (DMF, AR, ≥ 99.5%) and Triethanolamine (TEOA, 99.0~110.0%, AR) were chased from General-reagent. P25 was obtaining from Lijie Chemical Industry, Shanghai. Zinc nitratehexahydrate ($Zn(NO_3)_2.6\ H_2O$) was supplied from Shanghai Richjoint Chemical Reagents. Nano titanium powder (99.9%, metal basis, 300 mesh) was chased from Alladin-reagent. All chemical reagents were without further purificated. Deionized (DI) water was used throughout this work. $^{13}CO_2$ was provided by Sigma–Aldrich.

2.2. Catalyst prepration

2.2.1. Synthesis of ZN-TC

Zn, N co-doped TiO nanoparticles with carbon coating, denoted as ZN-TC, was synthesized by one-step calcination method with ammonia gas. Firstly, 0.5 g PAN was dissolved in 100 ml DMF, stirred at room temperature until clear and transparent. Then, 0.1 g P25 was added and scattered through Lewis acid-base interactions with DMF. After stirred 1 h, the mixture were transferred into a three-necked flask and n mmol (n = 1, 2, 3, 4, 5) $Zn(NO_3)_2.6\ H_2O$ was added in. The mixture was heated at 100 ℃ with the rotating speed of 400 rpm until the solvent was completely evaporated. It is worth noting that the heating environment needs to be insulated from oxygen, otherwise DMF will react with P25 to form dimethylamine (DMA). Finally, the dried sample was placed in a crucible and annealed in an ammonia atmosphere to reduce TiO_2 into TiO. The calcination conditions were as follows: firstly, the temperature was increased to 200 ℃ at a heating rate of 1 ℃/min and kept for 1 h to promote the cyclization and dehydrogenation reaction of PAN to form π-conjugated carbonaceous system with cyclized ladder structure; secondly, the temperature was increased to 600 ℃ at a heating rate of 2 ℃/min and kept for 2 h to make TiO_2 produce more structural defects, thereby reducing the TiO synthesis barrier and zinc doping barrier; finally, the temperature was increased to 800 ℃ at a heating rate of 3 ℃/min and kept for 3 h to prepare TiO. Since the boiling point of zinc is 907 ℃, the reduction temperature cannot be too high, otherwise it will cause meaningless zinc loss.

2.3. Synthesis of TiO

The cubic titanium monoxide nanoparticles, TiOx ($0.92 < x < 1.19$), were prepared by metal-reduction method according to previous work. Typically, p25 and nano titanium powder (300 mesh) were mixed at a molar ratio of 1:1.1. After milled at 350 rpm for 1 h, they were vacuum sealed to $5x10^{-3}$ Pa. The sample were finally at 900 ℃ for 24 h with the heating rate of 1 ℃/min.

2.4. Synthesis of Zn-TiO

Zn doped TiO, named Zn-TiO, was prepared of the mixture of pure TiO and zinc source. Typically, 0.1 g TiO nanoparticles was dissolved in 10 ml DMF, stirred at room temperature for 1 h. Then, 0.8 g $Zn(NO_3)_2.6\ H_2O$ was added and stirred for 6 h. The mixture was centrifuged and vacuum dried at 60 ℃ for 12 h. Finally, the powder was calcined at 350 ℃ in Ar atmosphere for 1 h.

2.5. Catalyst characterizations

The obtained sample was characterized by X-ray diffraction (XRD, Burker-AXS D8 Advance, German) in the angular of 30° to 80° in 2θ angle with Cu k_α radiation. The microstructure investigation was collected by the field emission scanning electron microscopy (FESEM, JEOL, FEG-XL30S, Japan) and the Transmission electron microscopy (TEM, JEOL, JEM-2100 F, Japan). The Raman spectra was obtained using a Horiba OLYMPUS BX41 with 633 nm laser excitation at 100% power. The X-ray photoelectron spectroscopy (XPS) was performed on an electron spectrometer (ESCALAB 250XI, Thermo, USA). The powder diffuse reflection spectra were tested by the UV–vis diffuse reflectance spectra (UV–vis–DRS) on a spectrophotometer (Shimadzu, UV-2401PC) with $BaSO_4$ as white reference. All the photoelectrochemical measurements were performed on a IVUIM electrochemistry workstation. Photoluminescence (PL) image was recorded on RF-5301 PC. Room-temperature electron spin resonance (EPR) spectra obtained using an EMX-8 EPR spectrometer (Bruker, German). The nitrogen adsorption-desorption isotherms (Micromeritics, USA) under liquid nitrogen (−196 ℃) were measured on a Quantochrome Autosorb-1 MP sorption analyzer with prior degassing under vacuum.

2.6. Photocatalytic CO_2 reduction experiment

The NIR-driven photocatalytic performance of ZN-TC nanoparticles were evaluated by photo-reduction of CO_2 (CO_2RR). Photocatalytic total CO_2RR reductions were carried out in a gas-tight circulation system (Labsolar 6 A, PerfectLight). Prior to the reaction, 20 mg of ZN-TC samples was dispersed within 90 ml DI water and 10 ml TEOA with stirring for 0.5 h. After completely degassing (−0.1 MPa) in the reactor, 80 kPa of CO_2 was injected, and the suspension was irradiated with a 300 W xenon lamp (PLS-SXE300D) equipped with a 420 nm or 780 nm cut-off filter. During the irradiation, the reaction suspension was kept at

20 °C by circulating cooling water.

An on-line gas chromatograph equipped with two flame-ionized detectors (FIDs) and a thermal conductivity detector (TCD) (GC-2014, Shimadzu) was used to analyze the evolved gases such as C_1 and C_2 productions every hour, and Ar was used as the carrier gas. The isotopic test was qualitatively examined by GCMS-QP2020 NX (Shimadzu). All products were detected by SH-Rtx-Wax column (30 m, 0.25 mmID, 0.25 μm df). The $^{13}CO_2$ was purged for 1 min and the reaction was performed under identical conditions with the reaction system described above.

The specific recycling test operation details are as follows: after the reaction, the catalyst and reaction medium are collected in a centrifuge tube and centrifuged for cleaning (16,000 rpm, 5 min, washed with ethanol and deionized water 3 times respectively). The sample is then vacuum dried to avoid air oxidation. Before the test, the catalyst needs to be re-weighed, and then repeat the CO_2 photocatalytic test procedure.

2.7. Photoelectrochemical characterization

The three-electrode method was used to test the NIR-driven photocurrent of ZN-TC nanoparticles. 0.5 M Na_2SO_4 (Aladdin) aqueous solution was selected as the electrolyte, Pt and Ag/AgCl electrode were used as counter electrode and reference electrode, respectively. 7.5 mg ZN-TC powder sample was dispersed in 0.5 ml of ethanol and 1 ml of α-terpineol, then 0.5 ml above dispersion was spin-dropping on a fluorine-doped tin oxide (FTO) glass (1 cm * 1 cm). Visible and NIR light can be achieved using 420 nm and 780 nm cut-off filters. In the process of recording the photocurrent response, there was no bias potential and the interval between on and off was 10 s. The LSV curve was performed at a scan rate of 10 mV s^{-1}. The EIS curve used the OCP as the starting voltage, the test frequency was $2 \times 10^6 \sim 1 \times 10^{-2}$, and the amplitude was 0.02 V.

2.7.1. CO_2 reduction products yield rate calculation

$$\textbf{Product yield rate}\left(\mu mol \cdot g^{-1} \cdot h^{-1}\right) = \frac{\left(C_{final} - C_{initial}\right) \times \textbf{volume of product mixture}}{\textbf{Amount of catalyst } (g) \times \textbf{Reaction time } (h)} \times 100\%$$

where C is the concentration of the product.

2.7.2. CO_2 Reduction Products Selectivity Calculation

$$CO(\textbf{selectivity } \%) = \frac{CO \text{ yield} \times 2}{CO \text{ yield} \times 2 + CH_4 \text{yield} \times 8 + C_2H_4 \text{ yield} \times 12 + C_2H_6 \text{ yield} \times 14} \times 100\%$$

$$CH_4(\textbf{selectivity } \%) = \frac{CH_4 \text{ yield} \times 8}{CO \text{ yield} \times 2 + CH_4 \text{yield} \times 8 + C_2H_4 \text{ yield} \times 12 + C_2H_6 \text{ yield} \times 14} \times 100\%$$

$$C_2H_4(\textbf{selectivity } \%) = \frac{C_2H_4 \text{ yield} \times 12}{CO \text{ yield} \times 2 + CH_4 \text{yield} \times 8 + C_2H_4 \text{ yield} \times 12 + C_2H_6 \text{ yield} \times 14} \times 100\%$$

$$C_2H_6(\textbf{selectivity } \%) = \frac{C_2H_6 \text{ yield} \times 14}{CO \text{ yield} \times 2 + CH_4 \text{yield} \times 8 + C_2H_4 \text{ yield} \times 12 + C_2H_6 \text{ yield} \times 14} \times 100\%$$

2.7.3. Apparent quantum yield (AQY) Calculation

$$AQY(\%) = \frac{Number\ of\ reacted\ electrons}{Number\ of\ incident\ photons} \times 100\% = \frac{Number\ of\ moles\ of\ product \times Number\ of\ required\ electrons}{\frac{H \times A}{\frac{h \times c}{\lambda}}} \times 6.02 \times 10^{23}$$

where h is Planck's constant (6.626×10^{-34} J·s^{-1}), H is the incident light intensity (1000 W·m^{-2} for AM 1.5), A is the irradiation area, and c is the speed of light (3×10^{8} m·s^{-1}).

Apparent quantum yield (AQY) was calculated after 1 h of light irradiation of a specific wavelength. The xenon lamp was equipped with diverse band-pass filters to obtain different monochromatic lights (420, 550, 700 nm). The energy of single-wavelength light was measured by optical power meter.

2.8. In situ DRIFTS characterization

In-situ diffuse reflectance infrared spectrum of CO_2 chemisorption was tested on Thermofisher IS50 spectrometer equipped with Harrick accessories. The number of scans is 20, the resolution is 4 cm^{-1}, and the unit is absorbance. Before the test, a certain amount of catalysts were fully ground and put into the in-situ infrared diffuse reflection sample cell. The sample cell was first bubbled with Ar gas (25 ml/min) for 1 h, and then CO_2 (10 ml/min) was introduced. The background was scanned under dark reaction conditions and used as a baseline, and then data was collected periodically under the irradiation of a 300 W xenon lamp.

2.9. In situ Raman characterization

In-situ Raman spectrum of CO_2 chemisorption was tested on a Horiba OLYMPUS BX41 Raman instrument equipped with a 633 nm laser. The power is 100%, and the range is 200–2000 cm^{-1}. The in-situ Raman pool uses the type of K004 (Tianjin Aida). Before the test, 10 mg of catalysts were ultrasonically made into ink in a mixed solution (500 μl H_2O, 460 μl isopropanol, 40 μl Nafion), and then dropped onto a glassy carbon electrode (5 *5 mm) and dried naturally. The sample cell was bubbled with Ar gas (25 ml/min) for 1 h, and then CO_2 (10 ml/min) was introduced. The background was scanned under dark reaction conditions and used as a baseline. We used two 300 W xenon lamps placed on the left and right sides of the sample cell, and applied the light path to fully illuminate the electrode and minimize the interference to the Raman signals. Then the data is collected regularly under light irradiation.

2.10. DFT computational details

All the density functional theory (DFT) were conducted using the Vienna ab initio simulation package (VASP) [15] code to explore geometries and electronic properties of the (101) facet of TiO. The interaction between the ionic core and the valence electrons was described by the projector augmented wave (PAW) method [16]. The estimated cut-off energy value required to achieve plausible results is 500 eV. The exchange and correlation potential were described by the Perdew-Burke-Ernzerhof (PBE) [17] of generalized gradient approximation (GGA) functional. The TiO surface was modeled using the

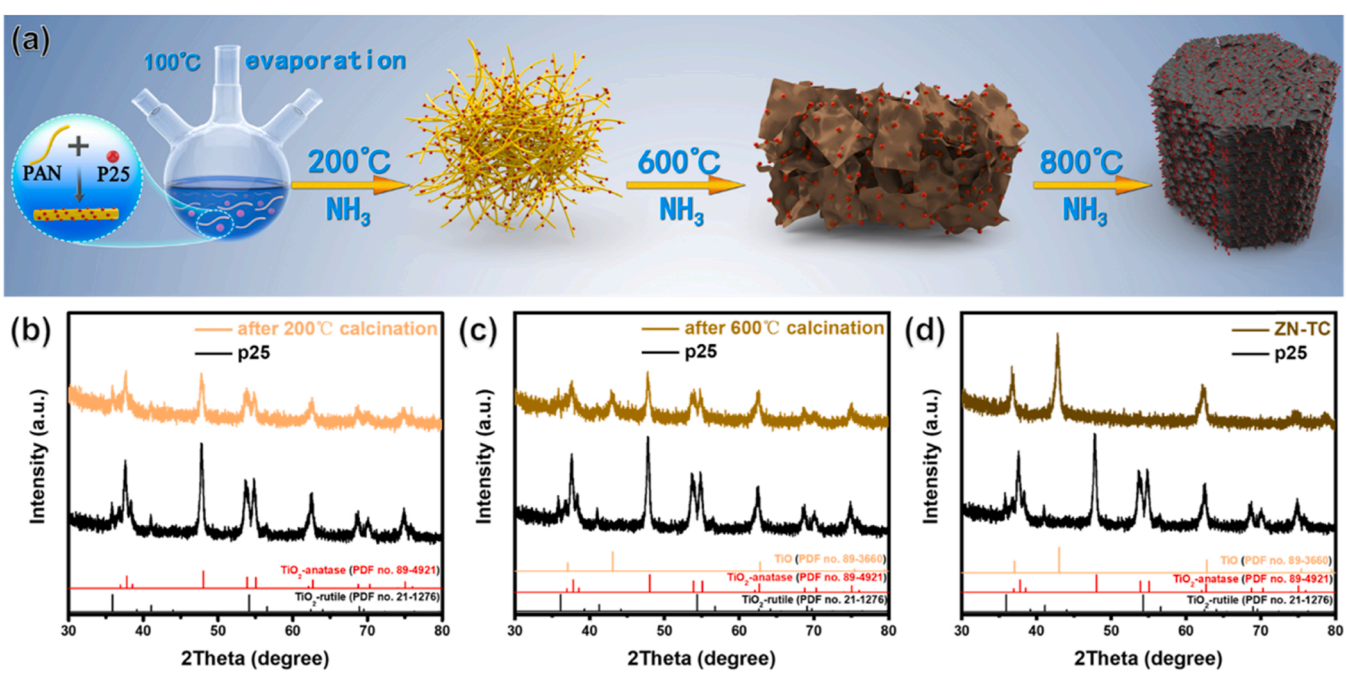

Fig. 1. (a) Schematic illustration of the synthetic process of ZN-TC. XRD pattern of the precursors: (b) calcined after 200 ℃, (c) calcined after 600 ℃ and (d) calcined after 800 ℃.

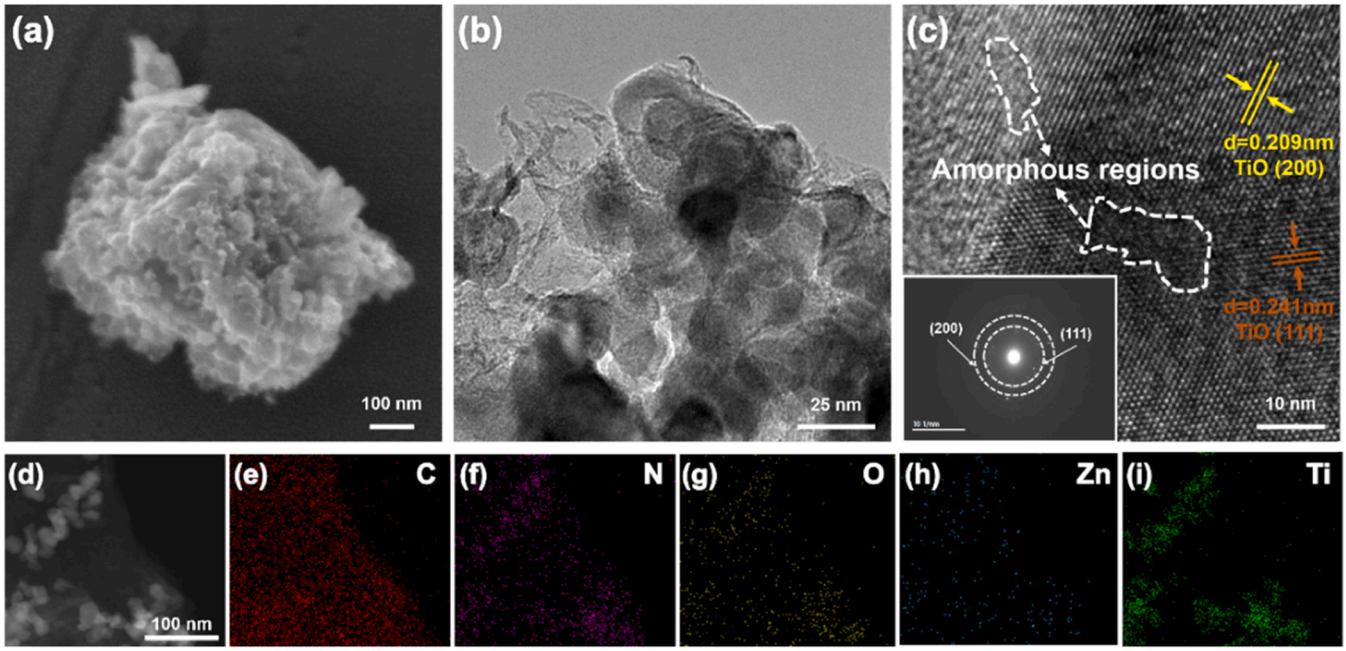

Fig. 2. (a) SEM, (b) TEM, (c) HRTEM and (d-i) Mapping imagines of N-TC. The insert in (c) is the SAED pattern.

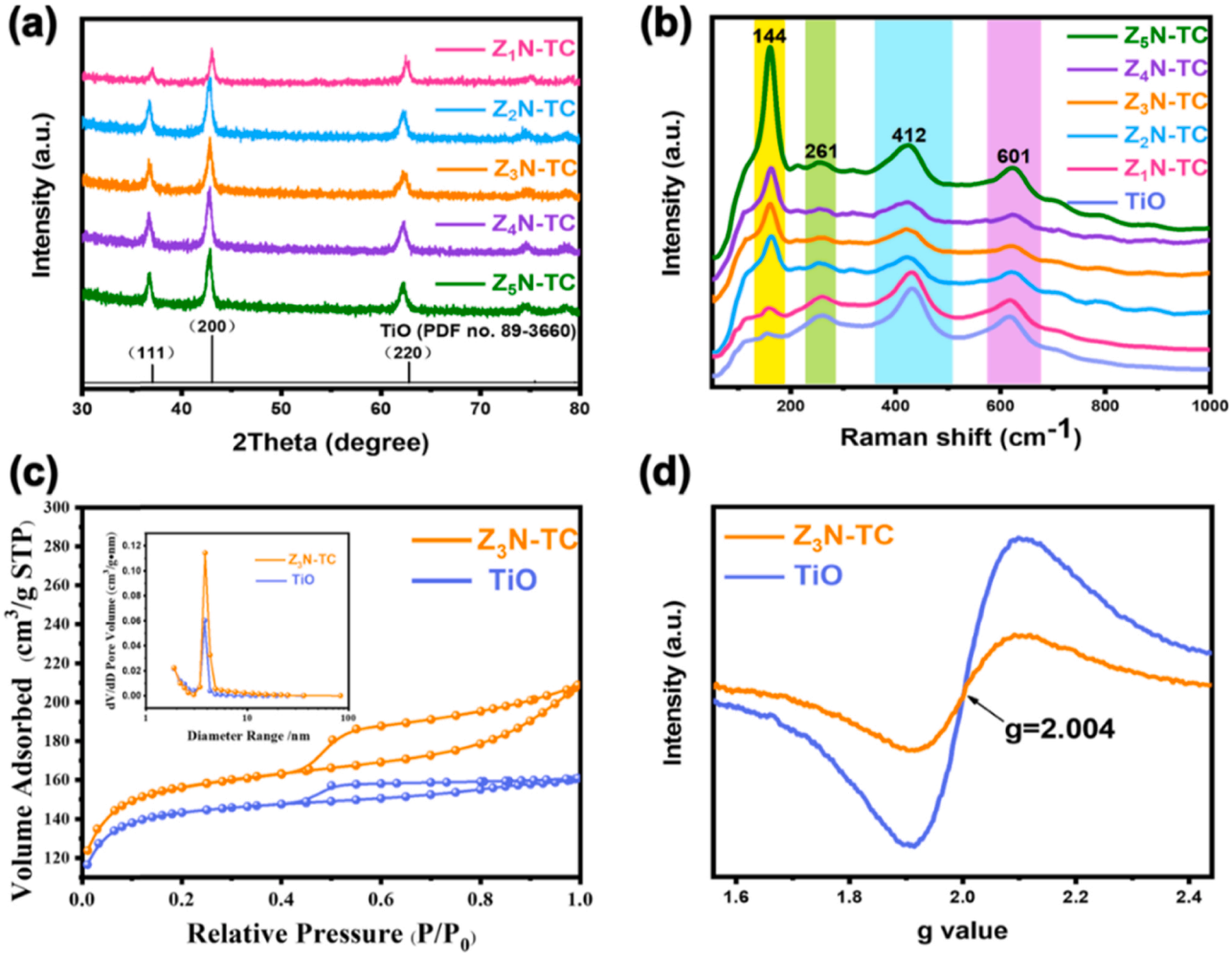

Fig. 3. (a) XRD patterns (b) Raman spectra of Z_XN-TC (x = 1, 2, 3, 4, 5). (c) N_2 adsorption-desorption isotherm curve of Z_3N-TC and TiO, inset: corresponding pore size distribution. (d) EPR spectra of Z_3N-TC and TiO.

stoichiometric slab structure where a vacuum layer of ~15 Å thick was added along the direction perpendicular to the surface to avoid interlayer interactions. The pristine TiO slab contained 12 at. layers, totaling 108 atoms: 54 Ti and 54 O atoms. The convergence criteria for the electronic energy and the geometry relaxation were set to 10^{-6} eV and 0.005 eV/Å, respectively. Electronic states were smeared using a Gaussian scheme [18] with a width of 0.1 eV. The k-point grid with densities of 0.2 $Å^{-1}$ was generated according to the Monkhorst–Pack scheme [19].

3. Results and discussion

3.1. Method development

In the Zn, N co-doped TiO (named ZN-TC) photocatalyst, the metallic TiO nanoparticles are selected as the plasmonic metal nanostructures with the aim of providing efficient photogenerated excitons. The graphite phase carbon layer coating is used to promote the rapid transmission of electrons, and the barrier between the sheets effectively inhibits the agglomeration of TiO nanoparticles during the calcination process. Furthermore, the Zn and N co-doping strategy successfully provides the elementary electric field to stabilize the ratio of active Ti^{3+}-Ti^{2+} pairs on the TiO through a charge compensation mechanism, thereby regulating the oxidation state of TiO.

The catalyst was achieved by the one-step reduction method (see Fig. 1a). Commercial TiO_2 (P25: 75% anatase crystal phase, 25% rutile crystal phase) was used as a TiO precursor, and DMF was selected as the solvent to enhance the dispersion of P25 in the solution, because of its good interaction with titanium ions through carbonyl groups due to the Lewis acidity of the Ti^{4+} center (Fig. S1) [20]. The polyacrylonitrile (PAN) could act as the origin of the graphite carbon and reducing agent, and also has good adsorption for zinc ions [21]. In the calcination process, three preservation platforms were set at 200 ℃, 600 ℃ and 800 ℃ for: (1) promoting the cyclization and dehydrogenation reaction of PAN [22], to form a conjugated carbonaceous system with a cyclization trapezoidal structure; (2) ensuring that NH_3 fully diffuses between conjugated layers of the graphite phase carbon and fully activates the TiO_2; (3) providing high temperature to promote the full reduction of TiO_2 to TiO. X-ray diffraction (XRD) tests (Fig. 1b) showed that the crystal phase of P25 had not changed at 200 ℃. After calcination at 600 ℃, the diffraction peak of the TiO (200) crystal plane appeared at 43.3° (Fig. 1c), which means that P25 starts to be reduced to TiO (JCPDS No. 89–3660) [23]. High-resolution TEM (HRTEM) also clearly captured the crystal lattice of TiO (Fig. S3), which is not found in the sample calcined at 200 °C (Fig. S2). After being treated at 800 ℃ for 3 h, P25 has been completely transformed into TiO (Fig. 1d).

3.2. Physical characterizations of the catalysts

As shown in scanning electron microscopy (SEM) and transmission electron microscopy (TEM) images (Fig. 2 and S4), the ZN-TC displays a massive lamellar stacking structure with an average particle size of ca. 20 nm for TiO particles. Such nanoscale sizes allow them to expose more Ti^{3+}-Ti^{2+} active sites. Besides, high-resolution TEM (HRTEM) image (Fig. 2c) shows the clear (111) crystal plane and (200) crystal plane of TiO, and some amorphous regions (the white circles) are found. This is likely to be due to the inevitable formation of defects during the calcination and doping process. However, select area electronic diffraction (SAED) (inset of Fig. 2c) demonstrates that ZN-TC still possesses a well-defined crystallinity. Energy-dispersive X-ray spectroscopy (EDS) images (Fig. 2d-i) confirm the existence of Zn and N with homogenous distribution. Furthermore, as shown in Table S1, the inductively coupled plasma optical emission spectrometer (ICP-OES) tests show that the Zn and N doping contents are maintained at about 1.2% and 2.33%, respectively.

Pure TiO nanoparticles were synthesized by the metal reduction method under high vacuum (Fig. S5), and their topographies are shown in Fig. S6. This bulk material possesses a particle size of ca. 400 nm, proving the function of the carbon layer to inhibit the agglomeration of TiO. For it could broaden the lattice structure by doping process, the clear (200) lattice spacing (0.208 nm) of pure TiO is slightly smaller than that of ZN-TC (0.209 nm) (Fig. 2c and S6e). Meanwhile, no (111) crystal plane is found near the amorphous regions of pure TiO. Although TiO has a good single crystal structure (inset of Fig. S6e), amorphous regions are still observed by HRTEM (the white circles). This phenomenon shows that the TiO material itself will inevitably undergo surface oxidation, and these amorphous regions may be the source of surface Ti^{3+}, and even Ti^{4+}, which will be discussed later. By comparing the differences between Fig. 2c and S6e, we speculate that the Zn, N co-doping mainly acts on the (111) crystal plane of TiO.

Next, we explored the influence of different Zn doping content on the material properties. The sample was named Z_XN-TC (x = 1, 2, 3, 4, 5) according to the amount of Zn^{2+} added. The inductively coupled plasma optical emission spectrometer (ICP-OES) tests show that the Ti/O ratio

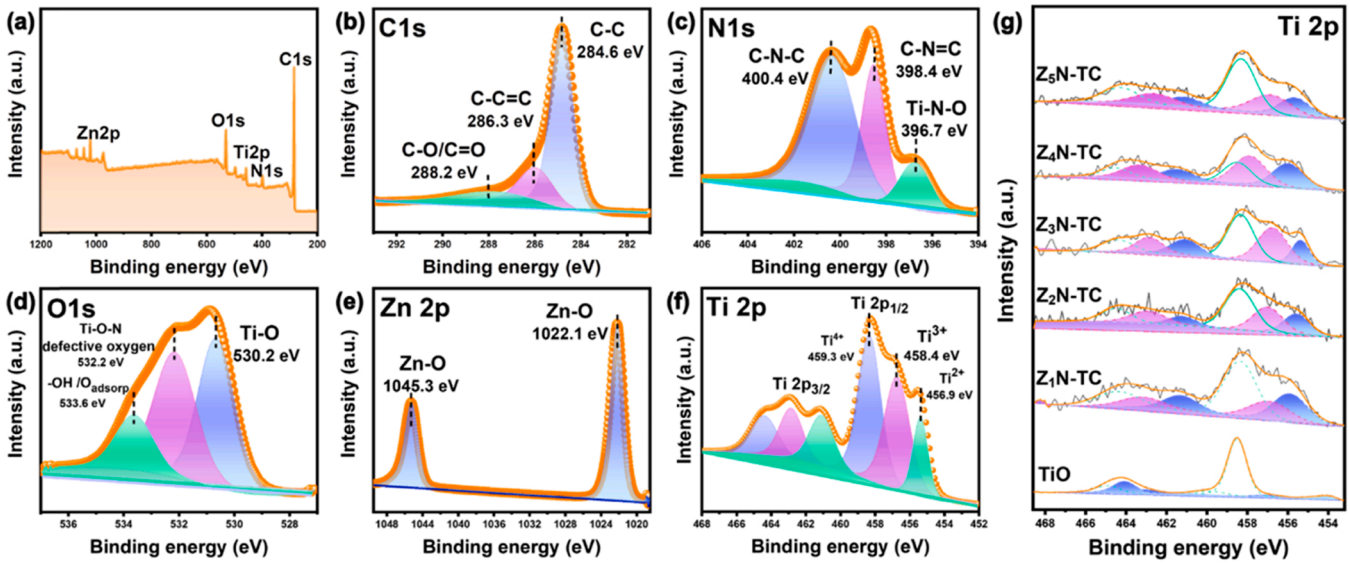

Fig. 4. Comparison of XPS spectra from Z_3N-TC samples. (a) Normalized survey spectra. (b) High-resolution XPS spectra of the C 1 s peak, (c) N 1 s peak, (d) O 1 s peak, (e) Zn 2p peak, (f) Ti 2p peak. (g) Normalized Ti 2p peaks with corresponding peak deconvolutions.

of all samples is maintained at about 1:1 (Table S2). XRD patterns of both Z_XN-TC and TiO samples were collected and analyzed to investigate the crystal structures, as shown in Fig. 3a and Fig. S7-S8. The three dominant peaks at 37.0°, 43.1° and 62.7° are well indexed to cubic TiO (JCPDS No. 89–3660), while no peak is detected for Zn or ZnO[21]. Besides, the diffraction peaks of Z_XN-TC are all slightly shifted to smaller degrees compared with TiO (Fig. S8), which is attributed to the widening and distortion of lattice spacing caused by the replacement of O by N and Ti by Zn, respectively. With increasing Zn content, the (111) peak and (200) peak shift gradually from 37.0° to 36.8° and from 43.0° to 42.8° (Fig. S8), respectively. The lattice parameters of Z_XN-TC, calculated by the Scherrer formula, are shown in Table S3. All samples display a disordered cubic phase (a=b=c), and Z_3N-TC has the smallest grain size (D) and slighter strain (0.552). This phenomenon might be related to the doping of Zn^{2+}, which changes the diffusion rate of TiO grain boundaries, thus controlling the growth rate of the TiO nuclei [24]. As a result, the grain size of TiO is adjusted, and appropriate defects are introduced at the same time. Three major peaks, located at 261 cm^{-1}, 412 cm^{-1} and 601 cm^{-1} in the Raman spectrum, also indicate the existence of TiO (Fig. 3b). Obvious broadening peaks at 412 cm^{-1} and a blue shift from 413 cm^{-1} to 408 cm^{-1} can be observed for oxidated titania compared with pristine Ti^{2+} [25]. The intensity of the E_g peak for TiO_2 at 144 cm^{-1} is also increased with Zn doping, confirming the inevitable mild oxidation of TiO. These results are in good agreement with the HRTEM images (Fig. 2c) and further confirm the formation of cubic TiO with low concentration doping. Moreover, ZN-TC also shows the peaks of the D and G vibration modes of graphite (Fig. S9), which are typically located at approximately 1347 cm^{-1} and 1591 cm^{-1}, representing the conjugated carbonaceous PAN after calcination. Due to the existence of the porous carbon layer, Z_3N-TC shows a higher specific surface area (555.8 m^2 g^{-1}) than TiO (443.6 m^2 g^{-1}) (Fig. 3c). It exhibits a type-IV isotherm, which indicates the presence of numerous mesopores of less than 50 nm, in accordance with the pore size distribution curve inset in Fig. 3c.

3.3. Electronic states and charge dynamics of the catalysts

We applied Z_3N-TC as the representative of ZN-TC. The surface electronic states were detected by electron paramagnetic resonance (EPR) spectra and X-ray photoelectron spectroscopy (XPS) spectra. In the EPR spectra (Fig. 3d), the characteristic unpaired electron signal at g= 2.004, which is associated with molecular oxygen from air trapped by the Ti^{3+} sites at the surface [10], can both be observed within Z_3N-TC and TiO. However, the EPR signal strength of Z_3N-TC is weaker than that of TiO, implying the substitution of part of the oxygen vacancies during doping with trivalent nitrogen ions.

XPS analyses were conducted to probe the oxidation states of the ions on the catalyst surfaces. As seen in Fig. 4a, five elements, C, N, O, Zn and Ti, are clearly displayed. The C elements are from calcinated PAN molecules and the adventitious element carbon. In the C 1 s spectra (Fig. 4b), the signal peak can be deconvoluted into three components at about 284.8 eV, 286.1 eV and 287.9 eV, respectively. The peak located at 284.8 eV is assigned to sp^3 C−C bonds of the conjugated carbonaceous system or adventitious elemental carbon, and the peak of 286.1 eV is related to sp^2 C-C═C bonds, while 287.9 eV corresponds to C-O and C═O bonds [26]. These results confirm that the conjugated PAN derivative with cyclized ladder structure is successfully formed. In addition, no Zn-C signal has been detected, ruling out the possibility of Zn doping into the carbon layers. The N 1 s XPS profile (Fig. 4c) shows three peaks at 396.7 eV, 398.4 eV and 400.4 eV, which are correlated to Ti-N-O bonds, pyridine nitrogen (C-N═C) and pyrrolic nitrogen (C-N-C), respectively [21]. In the O 1 s spectra (Fig. 4d), the sharp peak centered at 530.2 eV represents the lattice oxygen of Ti-O bonding in TiO [27]. Another major contribution at the higher binding energy of 532.2 eV leads to the Ti-O-N structure or defective oxygen (vacancies/defects) [38]. The third peak at 533.6 eV proves the existence of adsorbed oxygen (O_{adsorp}) or hydroxyl (-OH) [28]. The Zn 2p spectra displays two peaks at 1022.1 eV and 1045.3 eV [31], confirming the oxidation state of Zn^{2+} (Fig. 4e).

It is focused on the analysis of the oxidation state of the surface Ti element and how it is influenced by Zn, N co-doping. The detailed analysis data of each sample is shown in Table S4. As shown in Fig. 4f,

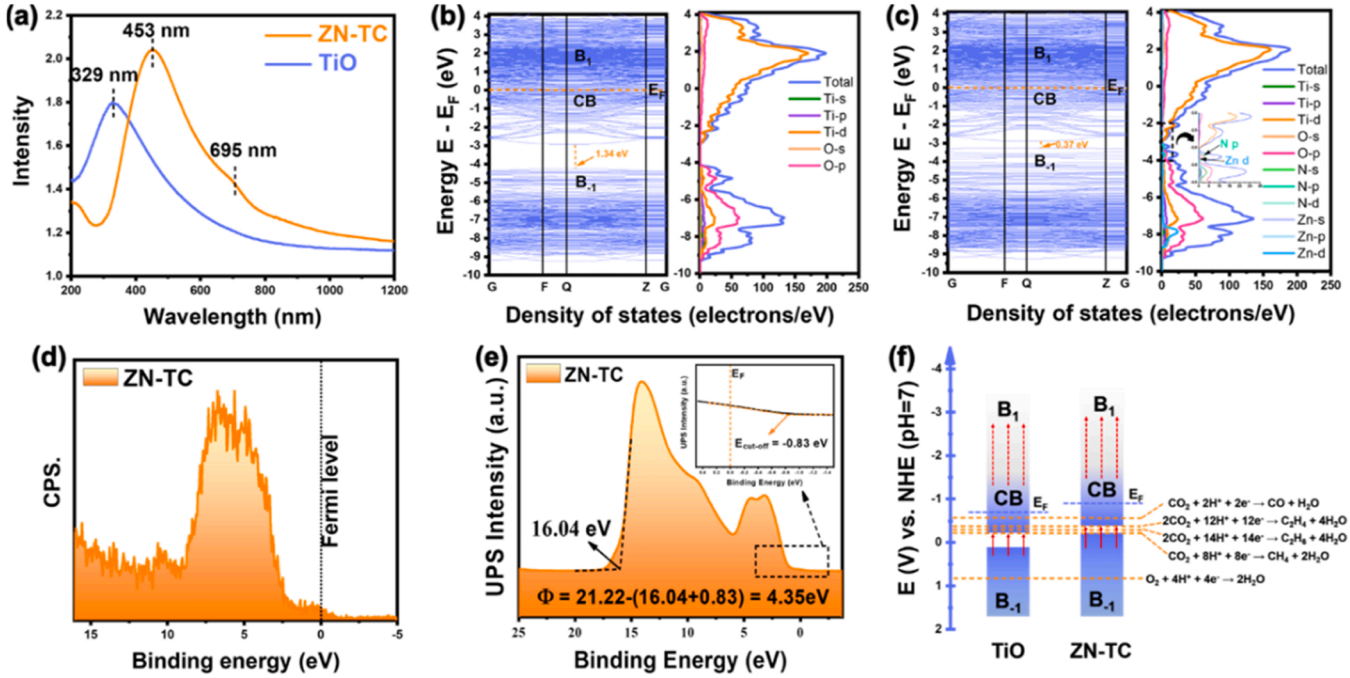

Fig. 5. (a) UV–vis–NIR diffuse reflectance spectra of catalysts. (b) and (c) The simulated band structure and DOS plots of TiO and ZN-TC. (d) Valence band XPS spectrum of ZN-TC. (e) Ultraviolet photoelectron spectrum (UPS) of ZN-TC. (f) The electronic band structure diagram of TiO and ZN-TC.

the Ti element on the surface can be deconvoluted into three components at about 455.5 eV, 457.4 eV and 458.5 eV, which represent the surface Ti^{2+}, Ti^{3+} and Ti^{4+}, respectively [27]. According to the HRTEM analysis (Fig. 2c and S6e) and Raman tests (Fig. 3b), Ti^{4+} may be derived from the inevitable surface oxidation in the air and the formation of defects introduced by doping during the synthesis process. Therefore, we further compared the differences in the oxidation state distribution of Ti among Z_XN-TC and TiO (Fig. 4g and Table S4). In TiO, Ti^{4+} occupies the vast majority of the proportion. Because XPS is a surface-sensitive technology whose sampling depth is only 1.5–4 nm for oxide samples, the XRD test results (Fig. 3a and S7) still remain as the pure TiO phase on the contrary. The binding energy of the Ti $2p_{3/2}$ orbital of TiO in Fig. 4g gradually shifts to lower energy with Zn, N doping, and the content of surface Ti^{2+} and Ti^{3+} increase at the same time, while maintaining a relative proportion. These phenomena demonstrate that Zn, N co-doping could regulate the local charge distribution of Ti atoms, suppressing large-scale oxidation of surface Ti^{2+} and leading to the formation of stable Ti^{3+} sites. Specifically, due to the low surface coverage of N, the elevated energy electronics in the 3d orbital of Ti^{2+} migrate to the 2p orbital of the adjacent N^{3-} through electronegativity differences, resulting in the formation of Ti^{3+} (confirmed by DFT calculation in Fig. 5). By contrast, the substitution of Zn^{2+} for Ti ions can stabilize the surrounding Ti^{2+} according to the principle of charge compensation. As it is low concentration doping, the Ti ions on the surface easily undergo oxidation once there are no Zn^{2+} or N^{3-} nearby, leading to the generation of Ti^{4+}. Therefore, the percentage of Ti^{2+} and Ti^{3+} on the Z_XN-TC surface are higher compared to TiO, which explains the downwards shift of the Ti 2p binding energy. Furthermore, the ratio of Ti^{3+}/Ti^{2+} among Z_XN-TC and TiO presents an obvious volcanic curve (Fig. S10). These results, taken together, reveal that Zn, N co-doping can modify the electronic structures of Ti sites, thereby modulating the oxidation state of TiO.

3.4. Band structure and optical properties

A typical photocatalytic CO_2 reaction involves four stages: (i) photon-adsorption, (ii) photogenerated carrier excitation and separation, (iii) CO_2 molecular adsorption and activation, and the later multi-proton coupling electron transfer process, (iv) product desorption at the active site. The first two stages are closely related to the inherent structure of the catalyst, while the latter two stages depend on the surface properties of the catalyst and the gas-solid or gas-liquid-solid multiphase interface in the actual reaction system. Therefore, we combined experimental characterization and theoretical calculations to further explore the photoelectric properties, band structure and surface properties of TiO-based catalysts.

Pure TiO powder shows off brown color, while that of Z_XN-TC powder is brown-black. This means that Z_XN-TC has better light absorption. In view of UV–vis–NIR adsorption spectroscopy (Fig. 5a), the average absorbance for TiO and Z_XN-TC are around 1.37 and 1.66, ranging from the UV to NIR region. The adsorption edge for TiO reaches 800 nm, with a significant LSPR peak at 329 nm. After doping with Zn and N elements, an obvious red shift occurs, both in the adsorption edge at 1200 nm and the LSPR peak at 453 nm. In addition, a new peak also appears at 695 nm. According to the results of XPS analysis (Fig. 4), this could be due to the change of Ti^{3+}/Ti^{2+} ratio on the surface, accounting for the movement of the local surface plasmon resonance (LSPR) peak and the appearance of the new peak. This is consistent with the local structural reorganization, which shows that the introduction of Zn^{2+} and N^{3-} can lead to the modulation of the TiO surface oxidation state.

To further uncover the band structures of TiO and ZN-TC, a theoretical calculation was carried out. The density of states (DOS) across the Fermi level reveals that both TiO and ZN-TC possess metallic behavior (Fig. 5b, c). Besides, the valence band XPS (VB-XPS) spectra passing through the Fermi level (0 eV) and the increasing resistivities, along with the elevating temperature, also verify their metallic nature (Fig. 5d, S11-S12). Unlike traditional semiconductor materials, the energy band composition of metallic photocatalysts includes three parts [29]: (1) a

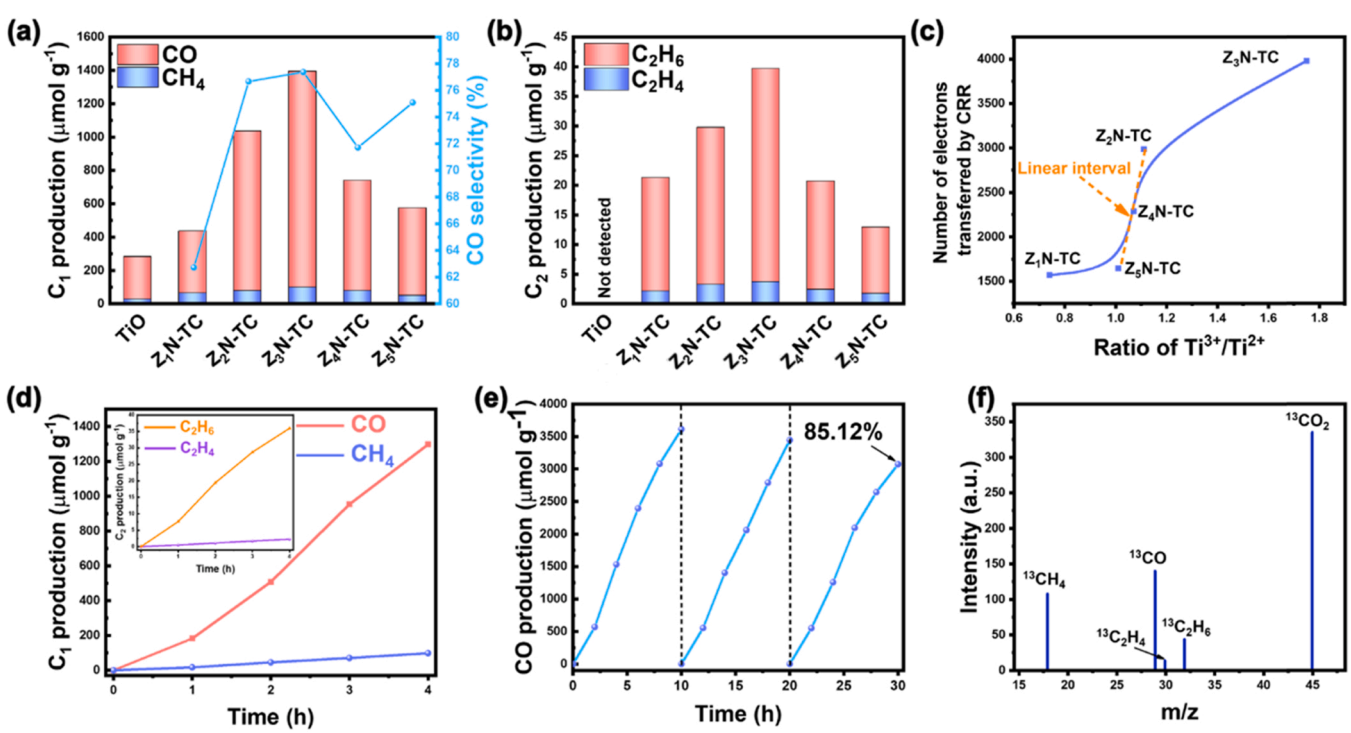

Fig. 6. (a) and (b) Photocatalytic CO_2 reduction performance of Z_XN-TC samples. The tests were carried out under visible irradiation ($\lambda > 420$ nm) for 4 h. (c) Correlation of Ti^{3+}/Ti^{2+} ratio with the number of electrons transferred by CO_2RR. (d) Formation rates of all products of Z_3N-TC under visible light ($\lambda > 420$ nm). (e) The recycling test of Z_3N-TC. (f) Isotopic measurement: mass spectra of indophenols in the solutions obtained by the reaction with $^{13}CO_2$.

series of energy levels completely filled with electrons are the B_{-1} band; (2) the energy band partially filled by electrons is called the CB band, which is commonly referred to the conduction band; (3) the energy band completely unfilled by electrons is the B_1 band. For the TiO (111) surface (Fig. 5b), the three parts are located between − 9.31 and − 4.26 eV (B_{-1}), − 2.92 and 0 eV (CB), and 0 and 4 eV (B_1), respectively. The metallicity of TiO mainly comes from the contribution of the Ti 3d orbital and the O 2p orbital. Due to the large number of oxygen vacancies inside and on the surface of the TiO crystals, the average valence state of the Ti element is low. This means that the Ti element has a higher electron density, which leads to the gradual transformation of the Ti-based suboxide to metallicity. When Zn and N are incorporated (Fig. 5c), the B_{-1} and CB bands for ZN-TC are located between − 9.34 and − 3.27 eV, and − 2.89 and 0 eV, respectively. As a result, the band gap between the B_{-1} and CB bands is reduced to 0.37 eV compared to 1.34 eV for pure TiO. Through further analysis, we found that this kind of co-doping strategy mainly acts on the upward shift of the orbital of the B_{-1} band. This effect mainly comes from the electronic contribution of the N 2p orbital to the B_{-1} band, which leads to the obvious upward splitting of the Ti 3d energy level, thereby broadening the B_{-1} band. In this process, Zn 3d orbitals also partly contribute, but this is not obvious. Thus, the above results confirm the previous analysis of co-doping to regulate the oxidation state of TiO: through the principle of charge compensation, electron-rich N^{3-} acts on the Ti 3d orbital, thereby producing a large amount of Ti^{3+}. Doping with divalent Zn ions maintains the stability of adjacent Ti elements. The two effects work synergistically to regulate the ratio of Ti^{3+}/ Ti^{2+}.

To evaluate the effect of metallic structure on photogenerated carriers and CO_2 activation, we characterized the photoelectric properties of the materials. Metallic catalysts can utilize the inter-band transition (B_{-1} → CB) or intra-band transition (CB → B_1) to excite hot electrons through the LSPR effect, thereby triggering CO_2 activation. ZN-TC has a lower inter-band gap (0.37 eV), which indicates that electrons are more likely to transition to the CB band at the edge of the B_{-1} band, thereby improving the CO_2 reduction performance. An ultraviolet photoelectron spectroscopy (UPS) test was applied to evaluate the dynamic performance of photogenerated electron migration (Fig. 5e). The ionization potential energy of Z_3N-TC was determined to be 3.07 eV under the excitation energy (21.22 eV), which is close to the band gap energy (2.89 eV) obtained from the theoretical calculation. This signifies that the energy required for electrons to migrate from the inside of the TiO crystal to the catalytic surface is low. Therefore, ZN-TC has a larger photocurrent and a smaller load transfer resistance (Fig. S13 and S14). A high carrier density but fast recombination rate is also a major challenge for metallic catalysts [30]. The lifetime of photo-generated carriers was measured by time-resolved transient PL decay spectra, and all data are listed in the inset of Fig. S15. The PL results for TiO and ZN-TC samples exhibit two components, including the shorter lifetime (τ_1) and the longer time (τ_2), with their corresponding percentage intensities (A_1%, A_2%). Typically, τ_1 is associated with nonradiative exciton recombination, such as the annihilation of positrons in the bulk of the catalyst, and τ_2 is associated with radiative exciton recombination [31]. Our characterizations show that both τ_1 and τ_2 increase with Zn, N co-doping, while the longest τ in Z_3N-TC possesses the lowest A_1% (8.44%) and

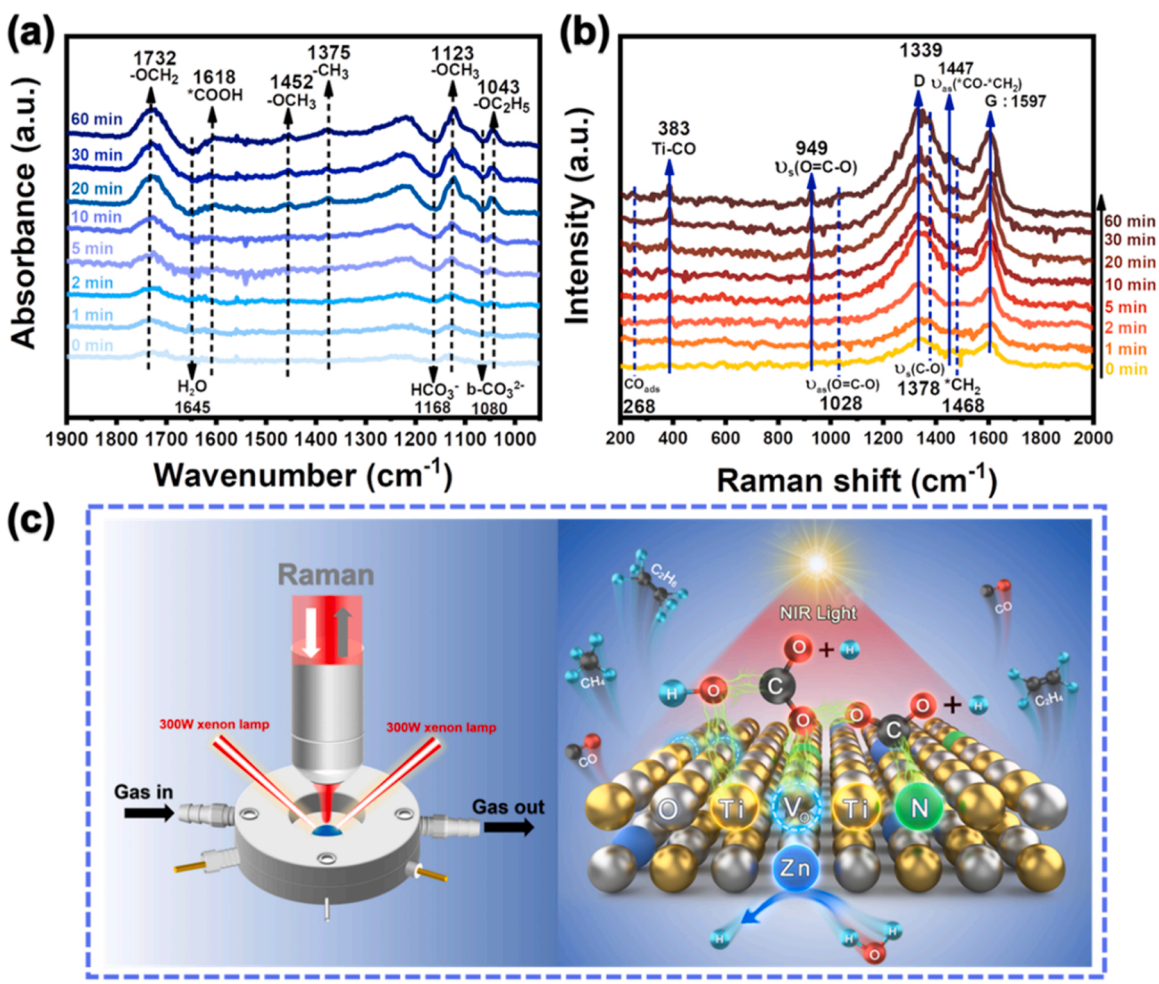

Fig. 7. In-situ DRIFTS (a) and in-situ Raman (b) for Z_3N-TC. (c) Schematic diagram of in-situ Raman model and photocatalytic CO_2 reduction performance over ZN-TC.

the highest A_2% (91.56%). This is because the co-doping strategy forms new defect centres to inhibit carrier recombination, although it can replace part of the oxygen vacancies, as analysed above. Ultimately, the electronic band structures of metallic TiO and ZN-TC are obtained, as shown in Fig. 5f.

3.5. Photocatalytic CO_2 reduction performances

Based on the above analyses, we then assessed the efficacy of Z_XN-TC for photocatalytic CO_2 conversion. The CO_2 conversion performance was carried out in a liquid/solid interfacial system under xenon arc lamp irradiation. As shown in Fig. 6a, pure TiO possesses certain CO_2 catalytic hydrogeneration performance and can produce CO and CH_4. Zn, N co-doping strategy modulates the local electronic structures of Ti, increasing the selectivity of CO and its yield. In Z_3N-TC, the CO production rate reaches 1296.45 μmol g^{-1} for 4 h reaction. Unlike TiO, all Z_XN-TC samples exhibit a C-C coupling function for C_2H_4 and C_2H_6 generation (Fig. 6b), indicating that Zn and N co-doping provides a new kind of C_2 product generation site. Both the yield rate of C_1 and C_2 products have a volcanic-curve correlation with Zn doped content. This co-doping strategy also significantly inhibits the competitiveness of the hydrogen evolution reaction (Fig. S16). In order to further explore the role of Zn and N, a pure Zn-doped TiO was prepared and named as Zn-TiO (Fig. S17). Photocatalytic tests show that this catalyst does not have the C-C coupling function (Fig. S18). Its CO yield is much higher than pure TiO, and its CH_4 yield is slightly higher than TiO. It is worth noting that the H_2 yield of Zn-TiO is higher than that of all samples. Thus, the introduction of pure Zn is likely conducive to the production of protons. Theoretical calculations have proved that Zn mainly acts on the B_{-1} band to enhance the hydrogen production capacity of solvent oxidation. Therefore, the test of Zn-TiO further supports the theoretical calculation inference in the experiment. Besides, the results of previous studies have proven that zinc element will change from 0 valence to positive divalence during the catalysis process [32–35]. This change is more conducive to the formation of π-back-bonding between Zn and *CO, which reduces the formation barrier of *COOH and *CO intermediates and promotes the generation of CO [35,36]. In addition, Zn atoms can also serve as catalytic sites for water reduction with lower activation energy [37]. Based on the experimental phenomena of this work and existing reports, Zn is more likely to be used as a stabilizer to stabilize Ti^{2+} and reaction intermediates, and N interacts with Ti for C-C coupling. The synergistic effect of the two promotes the continuous protonation of the intermediate and reduces the production of hydrogen.

It is noted that the number of electrons transferred by CRR are well correlated with the increased ratio of Ti^{3+}/Ti^{2+} (Fig. 6c), and the highest ratio of Ti^{3+}/Ti^{2+} in the best sample of Z_3N-TC displays the best performance. Coincidentally, the work of predecessors who tailored the ratio of Ti^{3+}/Ti^{4+} by C doped TiO_2 (C-TiO_X) proved that the photocatalytic nitrogen fixation performance of C-TiO_X has a linear relationship with the Ti^{3+}/Ti^{4+} ratio [10]. In this work, we explored the relationship between the ratio of Ti^{3+}/Ti^{2+} and other parameters (overall electron transfer number and each products' yield rate) (Fig. 6c and S19), and did not get an ideal functional relationship in the overall range. It is worth noting that all parameters show an approximate linear interval in the ratio range of 1.0–1.2. This phenomenon may be due to the different nature of the crystal structure of TiO and TiO_2. Although both are titanium oxides, it allows TiO to have a more uniform internal electric field through the high degree of symmetry from the unit cell brought by the cubic crystal system, and the low-valence Ti element ensures high carrier density. The existence of divalent Ti element may cause the coupling effect on trivalent and tetravalent titanium elements, so the conclusion that is applicable to the traditional tetragonal TiO_2 system does not produce same effect here.

The specific performance of Z_3N-TC is shown in Fig. 6d. Under visible light irradiation ($\lambda > 420$ nm) for 4 h, CO (1296.45 μmol g^{-1}), CH_4 (98.11 μmol g^{-1}), C_2H_4 (2.25 μmol g^{-1}) and C_2H_6 (41.07 μmol g^{-1}) can be well detected. C_2H_6 selectivity reaches 14.45% among all products. Under 420 nm light irradiation, its total apparent quantum yield (AQY) reaches 2.55% (Fig. S20). Control experiments confirm that both the nature of light and the photocatalyst are indispensable for these hydrocarbons (Fig. S21). To evaluate the near infrared (NIR) light catalytic activity, we applied a 780 nm cutoff filter and tested the CO_2 conversion rate of Z_3N-TC in isolation from outside light. As shown in Fig. S22, Z_3N-TC exhibits favorable NIR light catalytic activity, and the yield of CO monotonously increased with the extension of irradiation time. Notably, no other products (CH_4, C_2H_4 and C_2H_6) are detected in the reaction process, thus giving a 100% CO selectivity. As the photon energy of NIR light is less than 1.55 eV, it is not enough to support CO* for subsequent hydrogenation or C-C coupling. In addition, Z_3N-TC has excellent stability, remaining 85.12% activity after 30 h of testing (Fig. 6e). XRD and quasi in-situ XPS characterizations show that the crystal structure and surface electronic structure have not changed significantly during the reaction (Fig. S23 and S24), which further reflects the contribution of the Zn, N co-doping strategy to the oxidation state of Ti. To further validate the origin of the products, isotopic measurements (Fig. 6f) were applied and verified that C elements in all transformants originate from CO_2. Finally, we compared the ethane yield difference between Z_3N-TC and other Ti-based photocatalysts (Table S5). Even if no precious metal elements are added, Z_3N-TC still maintains good performance.

3.6. Mechanistic studies

Photocatalytic CO_2 reduction performance depends to a large extent on the interaction between the catalyst surface and CO_2 molecules with the type and quantity of intermediate active species. Herein, in-situ DRIFTS tests were applied to investigate the CO_2 intermediates. As shown in Fig. 7a and S25a, multiple fingerprint peaks, corresponding to adsorbed CO_2 molecules and their derived intermediates, were recorded in the DRIFTS spectra once the sample was exposed to light radiation. In general, the CO_2 intermediate species on the surface of Z_3N-TC are relatively abundant. In pure TiO (Fig. S25a), only bicarbonate (HCO_3^-) at 1199 cm^{-1}, methoxy species (-CH_XO) at 1161 cm^{-1} and 1112 cm^{-1}, carboxylate species (*COOH) at 1647 cm^{-1} were observed [26,31,38]. These vibration peaks all appear in the spectrum of Z_3N-TC (Fig. 7a). The vibration peak intensities in Z_3N-TC are much more higher, indicating that the reaction rate of Z_3N-TC is faster than that of TiO. The high activity is contributed to the transport of electrons from the surface of the catalyst to the 2π* anti-bonding orbital of *CO_2 [39].

New vibration peaks were observed in the spectrum of Z_3N-TC, especially including the methyl species (-CH_3) at 1375 cm^{-1} and the ethoxy species (CH_3CH_2O-) at 1043 cm^{-1}, which are the standard intermediates of C_2 products (such as ethylene and ethane) [40]. The dissociation peak of bidentate carbonate (b-CO_3^{2-}) was also found at 1080 cm^{-1} [41]. When light irradiation is applied to the reaction system, the peaks of adsorbed H_2O molecules, HCO_3^- and b-CO_3^{2-} quickly sag downwards. These phenomena represent the production of protons, and the activation and conversion of CO_2 [3,39]. After reacting for 10 min, the intensity of each fingerprint peak reaches a certain value and remains unchanged, indicating that the reaction has passed the activation period, and each intermediate product is continuously accumulated, transformed, and desorbed. However, the CH_4 vibration peak at 1540 cm^{-1} is not observed in the spectrum, although both Z_3N-TC and TiO can produce CH_4. This may be due to the non-polar molecule model of CH_4, with a symmetric structure, and the fact that CH_4 is easily desorbed from the surface of the catalyst.

To further confirm the authenticity of the in-situ DRIFTS results, we applied in-situ Raman tests to eliminate background interference from a large number of substances in the reaction medium. The detailed operation process was shown in the experimental section and Fig. 7c. As shown in Fig. 7b and S25b, *COOH shows three signal peaks at 934 cm^{-1}, 1028 cm^{-1} and 1378 cm^{-1}, representing the symmetric

stretching vibration of O═C-O (ν_sOCO), the asymmetric stretching vibration of O═C-O (ν_{as}OCO) and the stretching vibration of C-O (νCO), respectively [42]. The peak at 1269 cm^{-1} is attributed to the symmetric stretching vibration for CO_2^- [43]. Both Z_3N-TC and TiO have the bond of Ti-CO at ~ 380 cm^{-1}, proving the active site of Ti and the generation of CO. Compared with the Raman spectrum of TiO, the signal peaks of Z_3N-TC are also more abundant and obvious, which further confirms its faster catalytic rate. The signal peaks symbolizing the ethoxy group are also detected at 1447 cm^{-1} and 1468 cm^{-1}, which represent the asymmetric stretching vibration of *CO-*CH_2 and CH_2 wagging, respectively [39,43].

Based on the above work, we made assumptions about the reactive sites and CO_2 reduction pathways over the ZN-TC catalytic system. The products of ZN-TC are CO, CH_4, C_2H_4 and C_2H_6, among which CO and C_2H_6 are the main products of C_1 and C_2, respectively. Since the CO_2 adsorption activation center is generally located at the metal site, there are three possible active sites in ZN-TC: (i) Ti^{3+}/Ti^{2+}; (ii) Zn; (iii) oxygen vacancies (Vo); (IV) N. Among them, (i) (iii) and (IV) have been confirmed to have CO_2 catalytic activity [44]. In this work, the surfaces of ZN-TC and TiO contain different degrees of Ti^{3+}/Ti^{2+} and oxygen vacancies (Vo). Through the performance analysis of TiO, the production of C_1 product is mainly due to the synergistic effect of Ti^{3+}/Ti^{2+} and oxygen vacancies (Vo): electron-rich oxygen vacancies (Vo) promote the adsorption of CO_2 by capturing oxygen atoms, and lead to Ti^{3+}/Ti^{2+} center for subsequent catalytic activation. However, pure TiO cannot produce C_2 products. The appearance of CH_4 indicates that Ti^{3+}/Ti^{2+} is beneficial to the hydrogenation reaction of CO_2, but it is not an efficient C-C coupling site. Therefore, the coupling process is derived from the assistance of Zn and N. The role of Zn has been discussed in the photocatalytic performance part, and it is likely to be used as a stabilizer to stabilize Ti^{2+} and reaction intermediates. N interacts with Ti for C-C coupling. Furthermore, no information peak relating to Zn was found in the analysis of in-situ DRIFTS and Raman spectra (Fig. 7). On the contrary, the electron-rich N element acts on the CB and B_1 bands of TiO to promote the catalytic reaction of CO_2 and C-C coupling.

The schematic diagram of photocatalytic CO_2 reduction performance over ZN-TC was shown in Fig. 7c. Its relevant production paths of C_1 products are as follows:

$$* + CO_2 + e^- \rightarrow *CO_2^- (ads) \quad (1)$$

$$*CO_2^- (ads) + H^+ + e^- \rightarrow *COOH \quad (2)$$

$$*COOH + H^+ + e^- \rightarrow *CHO/*CO \quad (3)$$

$$*CO \rightarrow CO\uparrow \quad (4)$$

$$*CHO + H^+ + e^- \rightarrow *CH_2O \quad (5)$$

$$*CH_2O + H^+ + e^- \rightarrow *CH_3O \quad (6)$$

$$*CH_3O + 3\,H^+ + 3e^- \rightarrow CH_4\uparrow + H_2O \quad (7)$$

The C_2 reaction path is more complicated. Photocatalytic C-C coupling pathway generally has three forms: oxalate pathway; glyoxal pathway; methyl radical pathway [50]. According to in-situ testing and analysis, we specifically infer the production paths of ethylene and ethane as follows:

$$*CHO + *CO + 6\,H^+ + 6e^- \rightarrow *OCH_2CH_3 + H_2O \quad (8)$$

$$*OCH_2CH_3 + 3\,H^+ + 3e^- \rightarrow C_2H_6\uparrow + H_2O \quad (9)$$

$$*OCH_2CH_3 + H^+ + e^- \rightarrow C_2H_4\uparrow + H_2O \quad (10)$$

4. Conclusion

In summary, we have confirmed that TiO-based materials can be utilized as near infrared (NIR) light driven photocatalysts through theoretical calculation and experimental tests. The prepared ZN-TC catalyst possesses metallicity and exhibits high activity to CO and C_2H_6 in aqueous solution under visible light irradiation. The selectivity of C_2H_6 can reach 14.45%. Based on the XPS characterization and DOS calculation, this high C_1 and C_2 activities come from the regulation of TiO surface oxidation state caused by Zn and N co-doping. Through the charge balance mechanism, divalent Zn ions and trivalent N ions respectively regulate the valence states of adjacent Ti elements, thereby maintaining the stability of surface Ti^{3+}/Ti^{2+} pairs. In-situ DRIFTS and in-situ Raman further prove that the regulation of this oxidation state promotes C-C coupling to produce ethoxy groups, thereby promoting the production of C_2H_6. This work provides new ideas for the design of powerful photocatalysts for CO_2 reduction reactions, which may provide more opportunities for its practical applications.

CRediT authorship contribution statement

Baoxin Ni: Data curation, Visualization, Writing – original draft preparation. **Hua Jiang:** Conceptualization, Methodology, Software. **Wenyao Guo:** Visualization, Software, Investigation. **Qunjie Xu**: Software, Validation. **Yulin Min:** Supervision, Writing – review & editing.

Declaration of Competing Interest

The authors declare that they have no known competing financial interests or personal relationships that could have appeared to influence the work reported in this paper.

Acknowledgements

This work was supported by the National Natural Science Foundation of China (22075174, 21671133), Technology Commission of Shanghai Municipality (18020500800, 18JC1412900, 19DZ2271100 and 19160712900), and International Joint Laboratory on Resource Chemistry.

Appendix A. Supporting information

Supplementary data associated with this article can be found in the online version at doi:10.1016/j.apcatb.2022.121141.

References

[1] G. Liu, F. Zheng, J. Li, G. Zeng, Y. Ye, D.M. Larson, J. Yano, E.J. Crumlin, J. W. Ager, Lw Wang, F.M. Toma, Investigation and mitigation of degradation mechanisms in Cu_2O photoelectrodes for CO_2 reduction to ethylene, Nat. Energy 6 (2021) 1124–1132.

[2] X. Zhi, A. Vasileff, Y. Zheng, Y. Jiao, S.Z. Qiao, Role of oxygen-bound reaction intermediates in selective electrochemical CO_2 reduction, Energy Environ. Sci. 14 (2021) 3912–3930.

[3] J.C. Zhu, W.W. Shao, X.D. Li, X.C. Jiao, J.F. Zhu, Y.F. Sun, Y. Xie, Asymmetric triple-atom sites confined in ternary oxide enabling selective CO_2 photothermal reduction to acetate, J. Am. Chem. Soc. 143 (43) (2021) 18233–18241.

[4] X. Chang, J. Li, H. Xiong, H. Zhang, Y. Xu, H. Xiao, Q. Lu, B. Xu, C−C coupling is unlikely to be the rate-determining step in the formation of C_{2+} products in the copper-catalyzed electrochemical reduction of CO, Angew. Chem. Int. Ed. (2021), https://doi.org/10.1002/anie.202111167.

[5] Z.Z. Wu, F.Y. Gao, M.R. Gao, Regulating the oxidation state of nanomaterials for electrocatalytic CO_2 reduction, Energy Environ. Sci. 14 (2021) 1121–1139.

[6] Q. Wang, X. Yi, Y.-C. Chen, Y. Xiao, A. Zheng, J.L. Chen, Y.-K. Peng, Electronic-state manipulation of surface titanium activates dephosphorylation over TiO_2 near room temperature, Angew. Chem. Int. Ed. 60 (2021) 16149–16155.

[7] Z.W. Wang, Y.Z. Shi, C. Liu, Y.Y. Kang, L. Wu, Cu^{+}–Ti^{3+} interface interaction mediated CO_2 coordination model for controlling the selectivity of photocatalytic reduction CO_2, Appl. Catal. B Environ. 301 (2022), 120803.
[8] J. Wang, H.-Y. Tan, Y. Zhu, H. Chu, H.M. Chen, Linking the dynamic chemical state of catalysts with the product profile of electrocatalytic CO_2 reduction, Angew. Chem. Int. Ed. 60 (2021) 17254–17267.
[9] S. Zhu, X.D. Li, X.C. Jiao, W.W. Shao, L. Li, X.L. Zu, J. Hu, J.F. Zhu, W.S. Yan, C. M. Wang, Y.F. Sun, Y. Xie, Selective CO_2 photoreduction into C_2 product enabled by charge-polarized metal pair sites, Nano Lett. 21 (5) (2021) 2324–2331.
[10] Q. Han, C.B. Wu, H.M. Jiao, R.Y. Xu, Y.Z. Wang, J.J. Xie, Q. Guo, J.W. Tang, Rational design of high-concentration Ti^{3+} in porous carbon-doped TiO_2 nanosheets for efficient photocatalytic ammonia synthesis, Adv. Mater. 33 (2021), 2008180.
[11] Y.C. Wan, H.J. Zhou, M.Y. Zheng, Z.-H. Huang, F.Y. Kang, J. Li, R.T. Lv, Oxidation state modulation of bismuth for efficient electrocatalytic nitrogen reduction to ammonia, Adv. Funct. Mater. 31 (2021), 2100300.
[12] B. Xu, G. Duan, X. Li, G. Ding, L. Han, S. Zhang, Highly efficient electrocatalytic CO_2 reduction to C_{2+} products on a poly(ionic liquid)-based Cu(0)-Cu(I) tandem catalyst, Angew. Chem. Int. Ed. (2021), https://doi.org/10.1002/anie.202110657.
[13] E. Gong, S. Ali, C.B. Hiragond, H.S. Kim, N.S. Powar, D.Y. kim, S. I, Solar fuels: research and development strategies to accelerate photocatalytic CO_2 conversion into hydrocarbon fuels, Energy Environ. Sci. (2022).
[14] Huachuan Sun, Ching-Wei Tung, Yang Qiu, Wei Zhang, Qi Wang, Zhishan Li, Jiang Tang, Hsiao-Chien Chen, Chundong Wang, Hao Ming Chen, Atomic metal–support interaction enables reconstruction-free dual-site electrocatalyst, J. Am. Chem. Soc. (2021), https://doi.org/10.1021/jacs.1c08890.
[15] G. Kresse, J. F, Efficiency of ab-initio total energy calculations for metals and semiconductors using a plane-wave basis set, Comput. Mater. Sci. 6 (1996) 6–50.
[16] P.E. Blöchl, Projector augmented-wave method, Phys. Rev. (1994) 50.
[17] J.P. Perdew, K. B, M. Ernzerhof, Generalized gradient approximation made simple, Phys. Rev. Lett. 77 (1996) 77–3868.
[18] M. Methfessel, A. T. P, High-precision sampling for Brillouin-zone integration in metals, Phys. Rev. B 40 (1989) 40–3621.
[19] J.D. Pack, H. J. M, "Special points for Brillouin-zone integrations"-a reply, Phys. Rev. B 16 (1977) 16–1749.
[20] J.L. Lin, Y.C. Lin, B.C. Lin, P.C. Lai, T.E. Chien, S.H. Li, Y.F. Lin, Adsorption and reactions on TiO_2: comparison of N,N-dimethylformamide and dimethylamine, J. Phys. Chem. C 118 (2014) 20291–20297.
[21] Y. Dou, A. Zhou, Y. Yao, S.Y. Lim, J.R. Li, W. Zhang, Suppressing hydrogen evolution for high selective CO_2 reduction through surface-reconstructed heterojunction photocatalyst, Appl. Catal. B Environ. 286 (2021) 119876–119883.
[22] Q. Luo, X. Yang, X. Zhao, D. Wang, R. Yin, X. Li, J. An, Facile preparation of well-dispersed ZnO/cyclized polyacrylonitrile nanocomposites with highly enhanced visible-light photocatalytic activity, Appl. Catal. B Environ. 204 (2017) 304–315.
[23] Z. Li, J. Zhang, B. Guan, D. Wang, L.M. Liu, X.W. Lou, A sulfur host based on titanium monoxide@carbon hollow spheres for advanced lithium–sulfur batteries, Nat. Commun. 7 (2016) 13065.
[24] P.E. Goins, W.E. Frazier, A model of grain boundary complexion transitions and grain growth in Yttria-doped alumina, Acta Mater. 188 (2020) 79–91.
[25] T. Barudzija, A.A. Gusev, D. Jugovic, M. Dramicanin, M. Zdujic, C. Jovalekic, M. Mitric, Structural and magnetic properties of mechanochemically synthesized nanocrystalline titanium monoxide, Hem. Ind. 66 (2012) 181–186.
[26] H. Shang, X. Wang, H. Li, Z.Y. Chen, J. Sun, Z.H. Ai, L.Z. Zhang, Oxygen vacancies promote sulfur species accumulation on TiO2 mineral particles, Appl. Catal. B Environ. 290 (2021), 120024.
[27] P. Simon, B. Pignon, B. Miao, B. Bouchet-Fabre, C. Reynaud, N. Herlin-Boime, N-doped titanium monoxide nanoparticles with TiO rock-salt structure, low energy band gap, and visible light activity, Chem. Mater. 22 (2010) 3704–3711.
[28] L. Wang, Y. Zhu, Y. Wen, Y. Li, H. Peng, B. Zhang, Regulating the local charge distribution of Ni active sites for the urea oxidation reaction, Angew. Chem. Int. Ed. 60 (2021) 10577–10582.
[29] X. Xu, C. Randorn, P. Efstathiou, J.T.S. Irvine, A red metallic oxide photocatalyst, Nat. Mater. 11 (2012) 595–598.
[30] X. Li, L. Liang, Y. Sun, Y. Pan, J. Zhu, Y. Xie, Ultrathin conductor enabling efficient IR light CO_2 reduction, J. Am. Chem. Soc. 141 (2019) 423–430.
[31] X. Li, W. He, C. Li, B. Song, S. Liu, Synergetic surface modulation of ZnO/Pt@ZIF-8 hybrid nanorods for enhanced photocatalytic CO_2 valorization, Appl. Catal. B Environ. 287 (2021) 119934–119943.
[32] A. Beck, M. Zabilskiy, M.A. Newton, O. Safonova, M.G. Willinger, J.A. van Bokhoven, Following the structure of copper-zinc-alumina across the pressure gap in carbon dioxide hydrogenation, Nat. Catal. 4 (2021) 488–497.
[33] Z. Liang, L.P. Song, M.Z. Sun, B.L. Huang, Y.P. Du, Tunable CO/H2 ratios of electrochemical reduction of CO_2 through the Zn-Ln dual atomic catalysts, Sci. Adv. 7 (2021) eabl4915.
[34] S. Song, H. Song, L. Li, S. Wang, W. Chu, K. Peng, X. Meng, Q. Wang, B. Deng, Q. Liu, Z. Wang, Y. Weng, H. Hu, H. Lin, T. Kako, J. Ye, A selective Au-ZnO/TiO_2 hybrid photocatalyst for oxidative coupling of methane to ethane with dioxygen, Nat. Catal. 4 (2021) 1032–1042.
[35] S. Li, S. Zhao, X. Lu, M. Ceccato, X.-M. Hu, A. Roldan, J. Catalano, M. Liu, T. Skrydstrup, K. Daasbjerg, Low-valence $Zn^{\delta+}$ ($0<\delta<2$) single-atom material as highly efficient electrocatalyst for CO_2 reduction, Amgew. Chem. Int. Ed. 60 (2021) 22826–22832.
[36] K. Chen, T. Jiang, T. Liu, J. Yu, S. Zhou, A. Ali, S. Wang, Y. Liu, L. Zhu, X. Xu, Zn dopants synergistic oxygen vacancy boosts ultrathin CoO layer for CO_2 photoreduction, Adv. Funct. Mater. (2021), 2109336.
[37] S.Q. Luo, H.W. Lin, Q. Wang, X.H. Ren, H.P. David, T. Nagao, Y. Xie, G.L. Yang, S. J. Li, H. Song, M. Oshikiri, J.H. Ye, Triggering water and methanol activation for solar-driven H_2 production: interplay of dual active sites over plasmonic ZnCu alloy, J. Am. Chem. Soc. 143 (31) (2021) 12145–12153.
[38] F. Li, X.Y. Yue, D.N. Zhang, J.J. Fan, Q.J. Xiang, Targeted regulation of exciton dissociation in graphitic carbon nitride by vacancy modification for efficient photocatalytic CO_2 reduction, Appl. Catal. B Environ. 292 (2021) (2021), 120179.
[39] K. Wang, J.B. Lu, Y. Lu, C.H. Lau, Y. Zheng, X.F. Fan, Unravelling the C single bondC coupling in CO_2 photocatalytic reduction with H2O on Au/TiO2-x: combination of plasmonic excitation and oxygen vacancy, Appl. Catal. B Environ. 292 (2021), 120147.
[40] W. Jiang, J. Low, K. Mao, R. Long, L. Song, Y. Xiong, Pd-modified ZnO–Au enabling alkoxy intermediates formation and dehydrogenation for photocatalytic conversion of methane to ethylene, J. Am. Chem. Soc. 143 (2021) 269–278.
[41] Y. Cao, L. Guo, M. Dan, P. Chen, F. Dong, Y. Zhou, Modulating electron density of vacancy site by single Au atom for effective CO_2 photoreduction, Nat. Commun. 12 (2021) 1675.
[42] W. Zhang, C. Xu, Y. Hu, C. Wang, J. Ma, Z. Jin, Electronic and geometric structure engineering of bicontinuous porous Ag–Cu nanoarchitectures for realizing selectivity-tunable electrochemical CO_2 reduction, Nano Energy 73 (2020) 104796–104807.
[43] Z. Pan, K. Wang, K. Ye, T. Yu, Y. Wang, S. Song, Intermediate adsorption states switch to selectively catalyze electrochemical CO_2 reduction, ACS Catal. 10 (2020) 3871–3880.
[44] C. Foo, Y. Li, K. Lebedev, T. Chen, S. Day, C. Tang, S.C.E. Tsang, Characterisation of oxygen defects and nitrogen impurities in TiO_2 photocatalysts using variable-temperature X-ray powder diffraction, Nat. Commun. 12 (2021) 661.